

Imaging and Tracking of Targets in Clutter Using Differential Time-Reversal Techniques

Ahmed E. Fouda* and Fernando L. Teixeira

*ElectroScience Laboratory, Department of Electrical and Computer Engineering,
The Ohio State University, Columbus, OH, USA*

(Received 2010)

Two time-reversal algorithms for identifying, imaging, and tracking moving targets in clutter are introduced. The first algorithm classifies existing scatterers into stationary vs. moving targets. Multistatic data matrices (MDMs) corresponding to successive radar acquisitions (snapshots) of the scene are recorded. Singular value decomposition of the (time-)averaged MDM provides information on stationary targets, whereas singular value decomposition of the differential MDM provides information on moving targets. The second algorithm yields real-time selective tracking of each moving target by means of differential time-reversal. It requires minimal processing and memory resources, and exploits distinctive features of time-reversal such as statistical stability and superresolution. Numerical simulations are used to illustrate the capabilities of the proposed algorithms in different scenarios involving clutter from discrete secondary scatterers and from inhomogeneous random medium backgrounds.

Keywords: Backprojection; Decomposition of the Time-Reversal Operator (DORT); differential time-reversal (TR); Multistatic data matrix (MDM); selective focusing; statistical stability; superresolution.

1. Introduction

Imaging and tracking of obscured targets are of interest in many applications including law-enforcement and search-and-rescue operations [1]. Microwave signals are excellent candidates for such applications as they possess better penetration capabilities compared with optical or infrared signals for scenarios involving through-wall imaging, heavy dust and/or smoke, buildings debris or thick vegetation [1, 2].

However, imaging obscured targets in clutter is still a challenging problem. Scattering from the target(s) of interest can be of the same order or even weaker than scattering from ambient clutter. Several techniques have been developed to mitigate the effect of clutter [3–6]. Probably the most precise way to account for the clutter is to iteratively reconstruct the background, then use it to image or track the required target [1]. However, this is too costly in many applications in particular those involving real-time detection/tracking/classification.

Time-reversal (TR) techniques [7–13] have shown to be very useful for applications in remote sensing and imaging utilizing either acoustic/elastic waves [8, 11] or electromagnetic waves [9, 10, 12, 13]. These techniques exploit the time invariance of the wave equation in lossless media under TR [14, 15]. When backscattered signals are time-reversed and re-transmitted into the actual physical medium (or an artificially synthesized medium) they tend to focus automatically on the source (or

*Corresponding author. Email: fouda.1@osu.edu

passive scatterer in the “echo” mode) location. This “automatic focusing” property is independent of the intervening medium. Indeed, TR harnesses multipathing to enhance focusing resolution beyond the classical diffraction limit. This feature is known as *superresolution* [16–20]. Another feature of TR is self-averaging under ultra-wideband (UWB) operation, meaning that, under certain conditions, imaging in random media is independent of a specific realization of the random medium, but depends only on its statistical properties. This is known as *statistical stability* [21–25].

Many techniques have been developed for through-wall moving targets detection and localization, among which is Doppler radar [26]. Its basic form is based upon a continuous sinusoidal signal transmitted from a single transmitter; the range of moving targets can be determined by inspecting the backscattering spectrogram. So, in a sense, it is merely a 1-D motion detector [1]. An array of transmitters can be used and backprojection can be combined with Doppler processing to provide 2-D and 3-D localization. This type of strategy has been employed in [27], where combined Doppler processing and spatial beamforming was used to track humans through walls. The sensitivity of Doppler radars increases with the frequency of operation. However, the attenuation offered by walls and other obstacles to electromagnetic waves increases rapidly with frequency [28] and this puts an upper bound to the radar sensitivity. Another technique for through-wall motion detection was developed in [29–31]. It utilizes a motion detection filter (which is a high pass filter in essence) to filter out stationary clutter. Recently, UWB TR has been applied in through-wall imaging [32, 33] and differential TR for through-wall moving targets localization was briefly considered in [33, 34].

The objective of this paper is to introduce and assess two new techniques for imaging and tracking targets in clutter using UWB TR. We first develop an algorithm for classifying existing scatterers into stationary vs. moving targets. Stationary targets may represent, for example, pillars, furniture, tree trunks, or any fixed clutter. Moving targets may represent moving persons or vehicles. Even though, in principle, estimation of targets’ materials and electrical sizes can also be made from the available data, we are limiting ourselves to point-like scatterers here. A brief consideration on extended targets (e.g. walls) characterization [35–37] is presented in the Appendix.

Next, we develop a tracking algorithm based on differential TR. The proposed algorithm has outstanding clutter rejection performance since it is a differential technique. It is fast, simple, and requires minimal processing as compared with Doppler processing. In addition, it exploits beam forming to focus on each of the moving targets individually. Thus, it has potential applicability in wireless communication covertness in cluttered environments [38, 39] with selective beams automatically tracking respective moving users. It can also be integrated with micro-Doppler processing [40] to further analyze the motion characteristics of each moving target. We present the mathematical formulation of the algorithm and study factors affecting its tracking sensitivity. Performance in the presence of clutter from discrete secondary scatterers and continuous random inhomogeneous backgrounds (“discrete” and “continuous” clutter) is evaluated via numerical simulations. The algorithm is shown to possess both superresolution and statistical stability properties of UWB TR. Finally, the algorithm is applied to track multiple targets.

Numerical simulations of the forward problem are carried out here using the finite-difference time-domain (FDTD) method [41]. The computational domain is truncated with perfectly matched layer (PML) [42] defined through stretched coordinates [43] to emulate an open space. **All simulation setups are two-dimensional and the grid utilized is uniform with spatial cell size $\Delta_s = 2.5$ cm.**

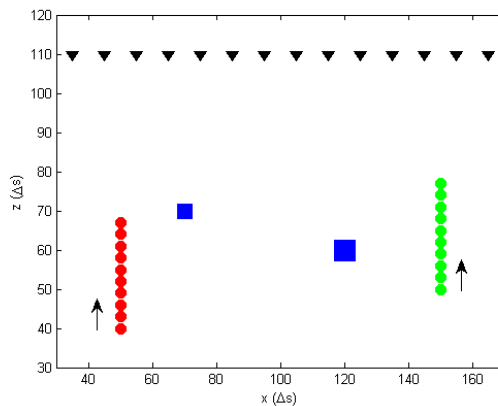


Figure 1. Problem layout: Two stationary targets (squares) and two moving targets (circles) at ten consecutive time instants. Left stationary: Metallic box with side length = $6\Delta_s$. Right stationary: Dielectric box with $\epsilon_r = 6$ and side length = $8\Delta_s$. Left moving: Dielectric box with $\epsilon_r = 6$ and side length = $8\Delta_s$. Right moving: Metallic box with side length = $6\Delta_s$. The directions of motion are indicated by black arrows and the positions of the 14 antenna array elements are indicated by black triangles.

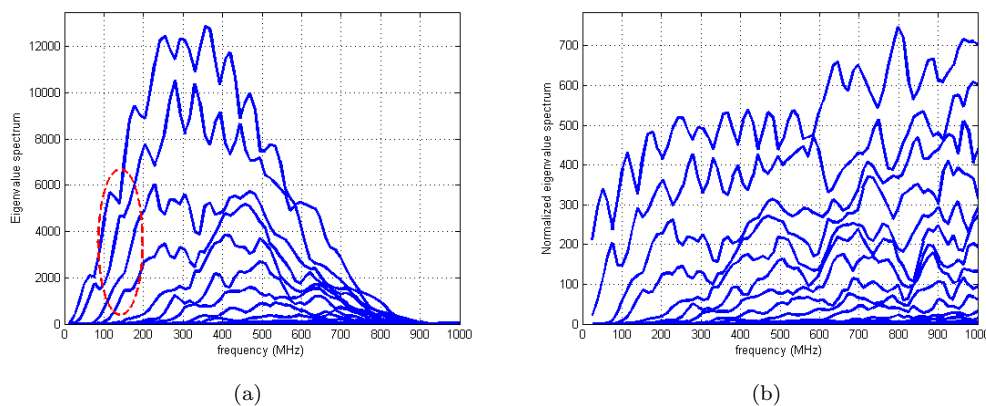


Figure 2. Spectrum of the eigenvalues of the TRO of the tenth snapshot. (a) Eigenvalues spectrum. (b) Normalized eigenvalues spectrum. Eigenvalues in (b) are normalized with respect to the input pulse spectrum. The spectrum of the first four eigenvalues is distinguishable from the remaining, especially from the behavior at the low-frequency end of the spectrum as indicated in (a). This reflects the presence of four point-like scatterers in the domain under investigation.

2. Stationary vs. moving targets discrimination algorithm

2.1. Problem scenario

Consider the setup shown in Fig. 1. Two point-like targets are moving upwards in the presence of two point-like stationary scatterers. The locations of the moving targets at four consecutive instants are indicated. The background is homogeneous with relative permittivity $\epsilon_r = 2$. The relative permittivity is chosen to coincide with the mean permittivity of scenarios involving continuously random background media, as considered later on (in practice, these scenarios correspond to imaging under fog, smoke, or heavy dust conditions, for example). A 14-element linear antenna array of y -polarized line sources is used. Consecutive array elements are separated by one half-wavelength.

Multistatic data matrices (MDMs) corresponding to each of the indicated locations are recorded. Recall that a MDM is obtained by successively firing a short pulse by each array element and recording the received signal by all elements [44, 45]. In our case, we use the first derivative of the Blackmann-Harris (BH) pulse [46] which has a center frequency $f_c = 400$ MHz and time duration $1.55/f_c$.

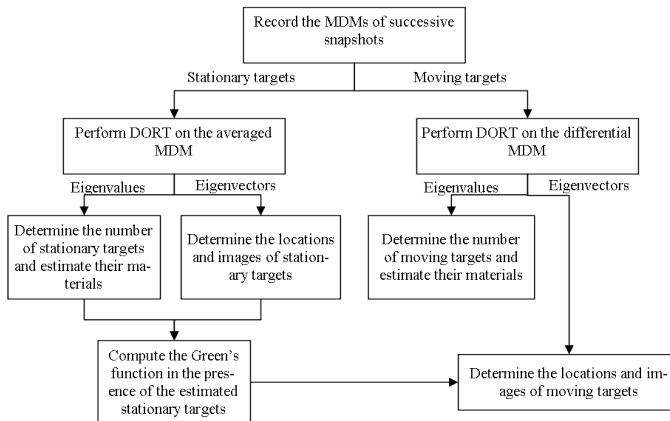


Figure 3. Fluxogram of the hierarchy for the discrimination algorithm with its two branches: stationary and moving targets detection.

It is assumed that the acquisition time required to record a MDM is much shorter than the other time scales of the problem. In particular, each moving target can be assumed still during an individual MDM acquisition. We call this acquisition a *snapshot*. The time interval between snapshots also needs to be sufficiently small so that the maximum displacement of moving targets (within the interval) is much shorter than the minimum wavelength of operation (in practice this criterion is also easily met with conventional electronics). This condition is necessary for accurately detecting moving targets as discussed in Section 2.3 below.

To analyze the contents of each snapshot, TR operators (TROs) of the recorded MDMs are computed for a discrete set of frequencies in the spectral window of the input signal. The TRO at frequency ω , $\mathbf{T}(\omega)$, is obtained from the MDM $\mathbf{K}(\omega)$ by $\mathbf{T}(\omega) = \mathbf{K}^\dagger(\omega)\mathbf{K}(\omega)$, where \dagger denotes conjugate transpose [45]. The “time-reversal operator decomposition” (DORT) method [24, 47–50] can be then applied to the TRO of each snapshot to obtain its eigenvalue/vector structure. As an example, the eigenvalue spectrum of the TRO of the tenth snapshot of Fig. 1 is shown in Fig. 2(a). This spectrum reflects the presence of four significant eigenvalues, corresponding to four well-resolved point-like targets. This can also be deduced from the normalized spectrum shown in Fig. 2(b).

The hierarchy of the discrimination algorithm is shown in Fig. 3. Having recorded several snapshots, the algorithm splits then into two separate processes: stationary target detection and moving target detection. Each process is described in detail below.

2.2. Stationary targets detection

The first step in stationary targets detection is to average out the recorded MDMs, then apply the DORT to the TRO of this (time-)averaged MDM. Since different MDMs capture moving targets at different locations, the contribution of moving targets to the eigenspectrum of the TRO of the averaged MDM is “washed out” after sufficient number of acquisitions. This enhances the relative contribution of stationary targets versus moving targets in the averaged MDM. Hence, the spectrum of the averaged TRO reflects the presence of only two significant scatters in this case, which are the stationary targets. This is shown in Fig. 4(a) and (b).

Images and locations of the stationary targets are obtained by projecting the eigenvectors associated with the significant eigenvalues of the average TRO on a synthesized imaging domain. Here we choose the imaging domain to be a homogeneous medium having the same permittivity as the actual background. The

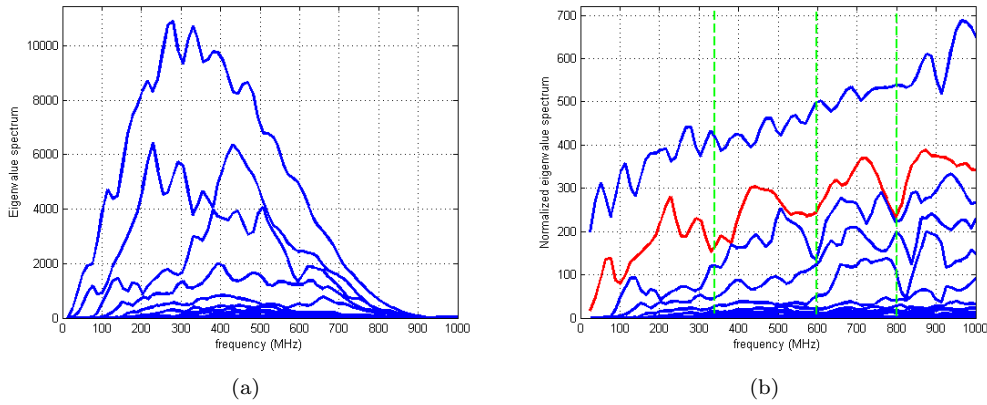


Figure 4. Spectrum of the eigenvalues of the TRO of the averaged MDM. (a) Eigenvalues spectrum. (b) Normalized eigenvalues spectrum. The spectrum of the first two eigenvalues is distinguishable from that of the rest, indicating the presence of two stationary scatterers. The vertical green-dashed lines in (b) point out the locations of the valleys in the dielectric target's response.

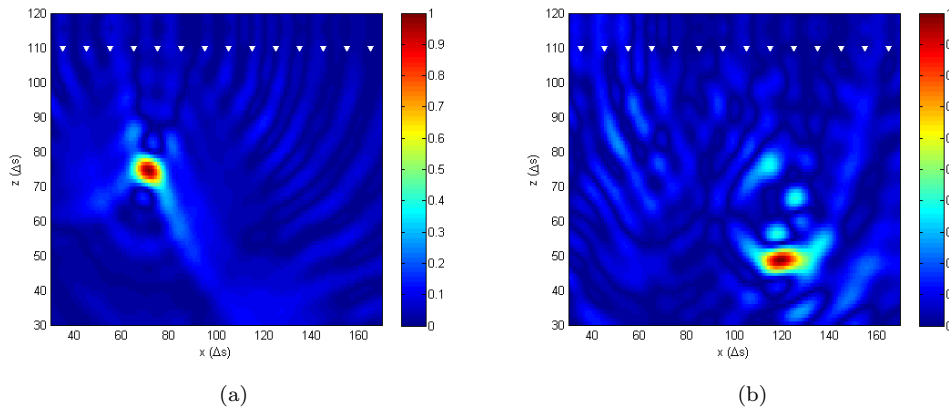


Figure 5. DORT images of the averaged MDM. (a) Image of the first eigenvector corresponding to the left stationary target. (b) Image of the second eigenvector corresponding to the right stationary target.

projection of the eigenvector \mathbf{q} on point p in the imaging domain at frequency ω is given by

$$P_p(\omega) = \left\langle \frac{\mathbf{g}_p(\omega)}{\|\mathbf{g}_p(\omega)\|}, \mathbf{q}(\omega) \right\rangle \quad (1)$$

where $\mathbf{g}_p(\omega)$ is the steering vector of point p , given by

$$\mathbf{g}_p(\omega) = [G_{(p,1)}(\omega), \dots, G_{(p,N)}(\omega)]^T \quad (2)$$

where $G_{(p,i)}(\omega)$ is the scalar Green's function between location p and the i^{th} element of the array, and N is the number of elements in the array. In addition, $\langle \mathbf{g}_k, \mathbf{q} \rangle = \mathbf{q}^\dagger \mathbf{g}_k$ denotes the inner product between \mathbf{g}_k and \mathbf{q} , where † refers to the conjugate transpose, and $\|\mathbf{g}_p(\omega)\|$ is the norm of \mathbf{g}_p given by $\|\mathbf{g}_p\| = \sqrt{\langle \mathbf{g}_p, \mathbf{g}_p \rangle}$.

To combine all frequencies, the projection in the time domain is computed by taking the inverse Fourier transform of $P_p(\omega)$, that is

$$P_p(t) = \mathcal{F}^{-1}(P_p(\omega)) \quad (3)$$

The focusing time t_f is defined as the time instant at which the peak of $P_p(t)$ over all points in the imaging domain occurs. Finally, the image at point p is given as

$$I_p = \left| \frac{P_p(t_f)}{\max_{\{p,t\}}(P_p(t))} \right| \quad (4)$$

The obtained images are shown in Fig. 5. It is apparent that the images coincide well with the actual targets locations.

Further information about the targets' size and/or composition can be extracted from their eigenvalue spectrum. By inspecting the spectrum we can infer whether the target is metallic or dielectric and, in the latter case, we can estimate its electrical size. The reflectivity of metallic scatterers with sufficiently high conductivity is almost frequency independent within the spectral range considered here. So, the eigenvalue associated with a metallic scatterer will have same spectrum as the input pulse. This can be seen in the spectrum of the first eigenvalue in Fig. 4(a), which is basically the spectrum of the first derivative of the BH pulse used as input. On the other hand, dielectric targets are penetrable so may act as imperfect resonators. Their reflectivity will possess periodic "peaks" and "valleys" experienced by such resonators. In the second eigenvalue in Fig. 4, we can observe the presence of a first valley at $f_v \approx 330$ MHz. From this value we can estimate the electrical length of the target along the co-range at the center frequency l_z/λ as $f_c/2f_v$, where l_z is the dimension of the target in the co-range direction, λ is the wavelength inside the dielectric target, f_c is the center frequency, and f_v is the frequency of the first valley. The previous relation follows directly from the simple null-frequencies formula of one-dimensional resonators. In our case, $f_v \approx 330$ MHz and $f_c = 400$ MHz, so the estimated electrical length $l_z/\lambda = 0.6$ agrees reasonably well with the actual value 0.65. A more detailed consideration of target characterization using DORT is presented in Appendix A.

Having estimated the locations/compositions of stationary targets, we can incorporate this information into a synthetic background for tracking of moving targets with increased accuracy [1]. This can be done as follows: a forward problem scenario is constructed where synthetic targets are positioned at the locations of the fixed targets with compositions and sizes chosen in virtue of estimated values. The forward problem is next solved numerically, from which the Green's function between each point in the domain and each array element can be computed and stored for use in the imaging of moving targets.

2.3. Moving targets detection

As opposed to the stationary targets detection algorithm, the goal of the moving targets detection algorithm is to enhance the contribution of moving targets in the eigenspectrum while suppressing that of stationary targets. Therefore, a reasonable procedure would be to compute the *differential* MDM i.e., the difference between the last two recorded MDMs. Since the displacement of moving targets between differenced snapshots is assumed much shorter than the wavelength, most of the contribution from stationary targets and multiple scatterings among moving and stationary targets cancel out under differencing. Therefore the eigenspectrum of the differential TRO will better correspond to the moving targets as shown in Fig. 6, where the two significant eigenvalues pertain to the two moving targets.

Backprojecting the respective eigenvectors of the differential TRO results in images that are located at some intermediate target locations between those of the last two snapshots. A mathematical analysis of this is presented in the next sec-

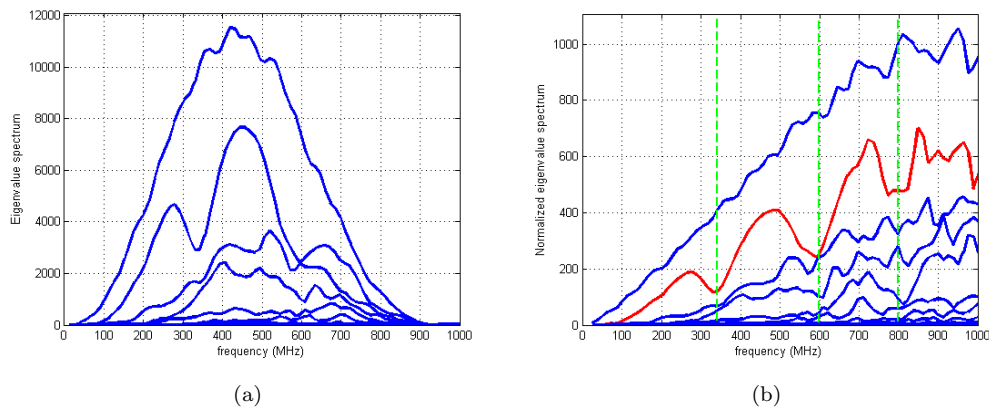


Figure 6. Spectrum of the eigenvalues of the TRO of the differential MDM. (a) Eigenvalues spectrum. (b) Normalized eigenvalues spectrum. The spectrum of the first two eigenvalues is distinguishable from that of the rest, indicating the presence of two moving scatterers. Again, the vertical green-dashed lines in (b) indicate the locations of the valleys in the dielectric target's response.

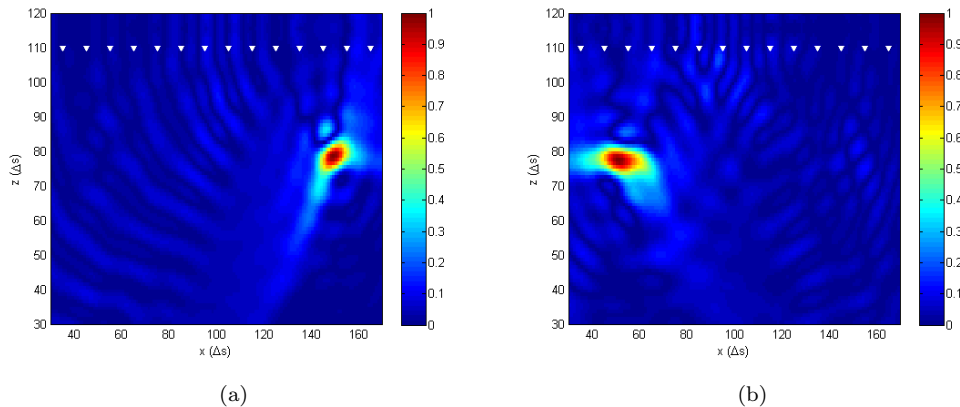


Figure 7. DORT images of the differential MDM. (a) Image of the first eigenvector corresponding to the moving metallic target. (b) Image of the second eigenvector corresponding to the moving dielectric target. The images are centered at intermediate locations between the tenth and the ninth snapshots.

tion on differential tracking. The resulting images are shown in Fig. 7. A similar analysis to the one used in Section 2.2 can be made to estimate the composition of the moving targets using their eigenvalues spectrum.

3. Time-reversal algorithms for tracking of moving targets

In this section we present the basic theory and discuss the performance of the proposed TR tracking algorithms. We start by presenting mathematical formulations for both non-differential and differential processings as well as contrasting their properties. It will be shown that non-differential processing is hampered by the presence of secondary scatterers. On the contrary, differential processing provides stationary clutter subtraction therefore enables higher tracking accuracy of obscured targets in rich scattering backgrounds. The performance of differential tracking in both discrete and continuous clutter is evaluated and the problem of tracking multiple targets is addressed.

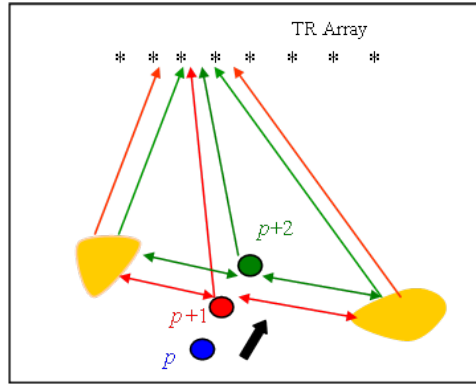


Figure 8. TR tracking approach. A target (circle) moves along the $p, p + 1, p + 2$ path in the presence of clutter (yellow objects). Rays indicating backscatterings from the target and clutter when the target is at location $p + 1$ and $p + 2$ are indicated by red and green arrows respectively.

3.1. Theory

Consider the setup shown in Fig. 8. A target is moving diagonally upwards as indicated by the arrow. Our goal is to track the motion of the target. Apparently the tracking algorithm has to be fast enough to respond to the target motion. The main limitation on the tracking speed comes from the processing time required to compute the target location after each snapshot acquisition. This is in fact the main deficiency of the discrimination algorithm presented in Section 2.3, since it involves the relatively expensive singular value decomposition of the acquired MDMs; therefore, it is less suited for real-time tracking. Nevertheless, it can be used to determine the initial locations of moving targets at some particular instant of time. From that point on, the tracking algorithm takes over and continues tracking each of the moving targets.

The idea behind the proposed tracking algorithm is to simultaneously excite array elements so as to provide a beam that selectively focuses on the moving target, rather than exciting each array element separately by the same input signal as done in the conventional MDM acquisition. Backscattering is recorded and processed as described below to yield the updated target location and the process is repeated. In cases where there exists more than one moving target, selective beams corresponding to each of the targets are fired successively. The acquisition time will be less than that of the MDM as long as the number of moving targets is less than the number of array elements.

3.1.1. Non-differential processing

Having determined the location of the target at a particular instant indicated by p in Fig. 8, a selective beam is launched in the physical medium. The input to the array is basically the time-reversed (phase conjugated in the frequency domain) steering vector of point p , \mathbf{g}_p given in (2). The incident beam illuminates the target at location $p + 1$, and the backscattering at frequency ω is proportional to the electric field received by the antenna array \mathbf{s}_{p+1} , given by

$$\mathbf{s}_{p+1} = \langle \mathbf{g}_{p+1}, \mathbf{g}_p \rangle \tau(\omega) \mathbf{g}_{p+1} + \mathbf{c}_{p+1} \quad (5)$$

where $\tau(\omega) = |\tau(\omega)| e^{j\Phi_{\tau(\omega)}}$ is the scattering coefficient of the target at frequency ω ; and \mathbf{c}_{p+1} is the backscattering collected by the array elements from the clutter when the target is at location $p + 1$. In order to guarantee that the target at location $p + 1$ is illuminated by the focused beam initially transmitted to focus at location p , namely \mathbf{g}_p , the time interval δt between successive illuminations has again to be

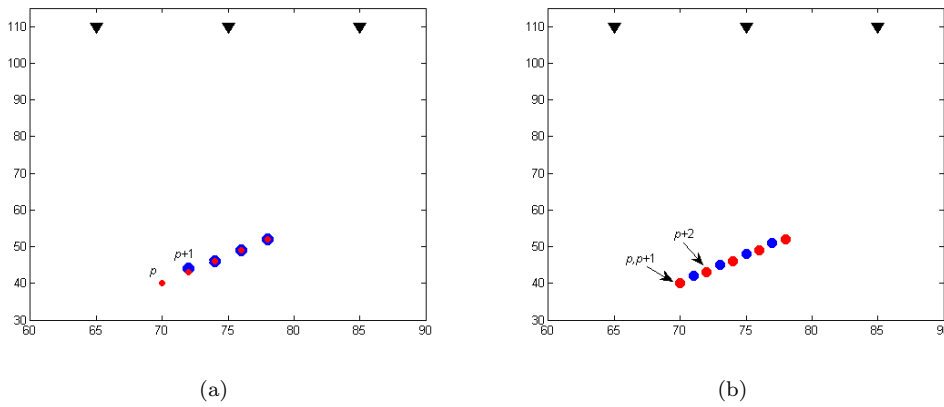


Figure 9. Actual (red) and detected (blue) traces for (a) non-differential tracking. (b) differential tracking. In both cases the target is moving ‘upwards’.

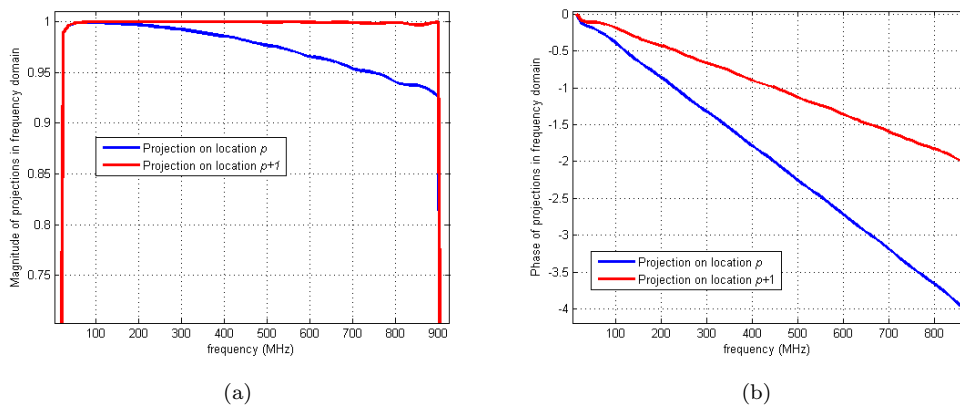


Figure 10. Non-differential processing projections, in the frequency domain, at locations p and $p+1$ indicated in Fig. 9(a). (a) The magnitude. (b) The phase.

short enough¹.

In scenarios where direct scattering from ambient clutter is negligible compared with the scattering from the target, the \mathbf{c}_{p+1} term in (5) can be neglected. This is an important assumption for non-differential processing to be able to trace the motion.

In order to detect the target’s image and location, the normalized phase conjugated scattering vector is projected onto the normalized steering vectors of a synthesized imaging domain. In the absence of any information about the imaging scenario, a possible choice of the imaging domain in this case would be a homogeneous medium with the same (estimated) average permittivity as the background of the forward problem setup. The projection onto location I in the imaging domain is given by

$$P_I = \left\langle \frac{\mathbf{g}_I}{\|\mathbf{g}_I\|}, \frac{\mathbf{s}_{p+1}}{\|\mathbf{s}_{p+1}\|} \right\rangle \quad (6)$$

where \mathbf{g}_I is the steering vector corresponding to location I in imaging domain. The

¹Suppose, for example, a (conservative) 3 dB margin such that location $p+1$ lies within the half-power beamwidth Ω_H of the beam (from \mathbf{g}_p). In this case, δt has to be less than $\Omega_H/\hat{\theta}_{max}$, where $\hat{\theta}_{max}$ is the maximum angular velocity of the target in cross-range.

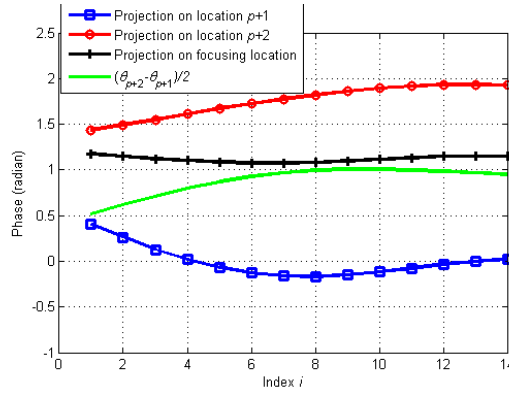


Figure 11. Phases of the the 14 terms composing the projections of the differential vector on the imaging domain at the center frequency of the considered bandwidth.

above projection can be expanded as

$$P_I = \sum_{i=1}^N \frac{G_{(I,i)} S_{(p+1,i)}^*}{\|\mathbf{g}_I\| \|\mathbf{s}_{p+1}\|} \quad (7)$$

where $S_{(p+1,i)}$ is the i^{th} component of \mathbf{s}_{p+1} and the $*$ denotes complex conjugation. The phase of the i^{th} term of the above sum can be written as

$$\Phi_{P_{(I,i)}} = -\alpha_{(p+1,p)} - \Phi_{\tau(\omega)} - \theta_{(p+1,i)} + \theta_{(I,i)} \quad (8)$$

where $\langle \mathbf{g}_k, \mathbf{g}_l \rangle = |\langle \mathbf{g}_k, \mathbf{g}_l \rangle| e^{j\alpha_{(k,l)}}$ and $G_{(m,i)} = |G_{(m,i)}| e^{j\theta_{(m,i)}}$.

The maximum value for the projection occurs when all of its components add constructively. This requires $\Phi_{P_{(I,i)}}$ to be independent of i . As seen from (8), this occurs only when $\theta_{(I,i)} = \theta_{(p+1,i)}$. In other words, the projection peaks at the location of the target when the latter is “hit” by the pulse initially emitted to focus on p , and this is how the tracking operates. The target location is updated and the process is repeated to detect the successive locations. To verify the previous analysis, non-differential processing is applied to track a target moving in homogeneous background. Actual and detected traces are shown in Fig. 9(a). It is clear from this figure that detected locations coincide with locations $p + 1$ of each $(p, p + 1)$ pair.

Magnitudes and phases of the projections on locations p and $p + 1$, indicated in Fig. 9(a), are plotted in Fig. 10(a) and (b) respectively. It is clear that $|P_I|$ at $p + 1$ has a value of one over all frequencies. This is the maximum value $|P_I|$ can take according to (6). Note that the projection P_I is almost coherent, i.e. it has almost linear phase progression with frequency. Some deviations from the linear behavior, especially at low frequencies, are observed. These deviations are due to the phase response of the complex scattering coefficient $\tau(\omega)$. In case of coherent (or near-coherent) projection, we can find the location of the maximum by looking for the point in the imaging domain that maximizes the magnitude of each frequency component as discussed above.

3.1.2. Differential processing

Consider the same setup as the previous section, where now the focused beam \mathbf{g}_p is transmitted twice at two closely separated time instants. The first transmission illuminates the target at location $p + 1$ and the backscattering is given by (5). Similarly, the second transmission illuminates the target at location $p + 2$ as shown

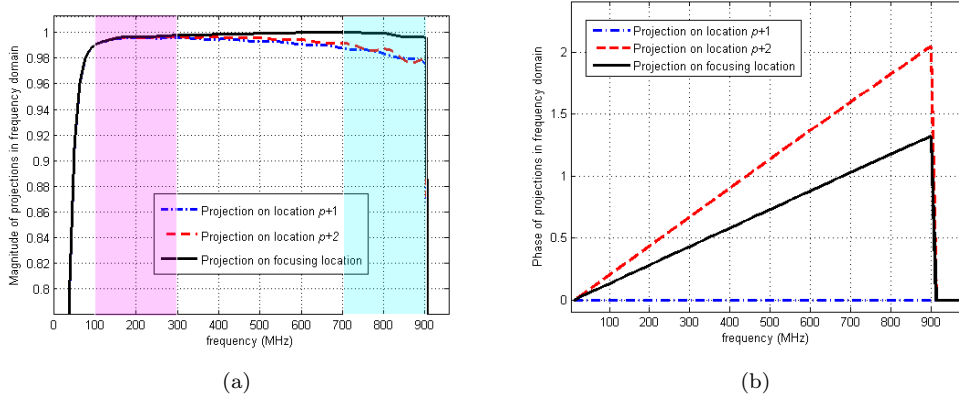


Figure 12. Differential processing projections, in the frequency domain, at locations $p + 1$, $p + 2$ and the intermediate focusing location indicated in Fig. 9(b). (a) The magnitude. (b) The phase. Highlighted frequency bands will be used later to study the traceability of the tracking algorithm.

in Fig. 8 and \mathbf{s}_{p+2} can be written as

$$\mathbf{s}_{p+2} = \langle \mathbf{g}_{p+2}, \mathbf{g}_p \rangle \tau(\omega) \mathbf{g}_{p+2} + \mathbf{c}_{p+2} \quad (9)$$

If the acquisition speed is chosen sufficiently faster than the target speed, we can safely assume that the distance between location $p + 1$ and location $p + 2$ is small. Thus the difference in the backscatterings from the clutter corresponding to the two locations is negligible. That is

$$\mathbf{c}_{p+1} \approx \mathbf{c}_{p+2} \quad (10)$$

Moreover, from the properties of the Green's functions, we can assume that the difference in the Green's functions affects mostly the relative phase, so that

$$|G_{(p+1,i)}| \approx |G_{(p+2,i)}| \quad (11)$$

and

$$|\langle \mathbf{g}_{p+1}, \mathbf{g}_p \rangle| \approx |\langle \mathbf{g}_{p+2}, \mathbf{g}_p \rangle| \quad (12)$$

We define the differential backscattering vector $\mathbf{d}^{(p+2,p+1)}$ as

$$\mathbf{d}^{(p+2,p+1)} = \mathbf{s}_{p+2} - \mathbf{s}_{p+1} \quad (13)$$

Substituting with (5) and (9) and using (10), (11) and (12), the i^{th} component of $\mathbf{d}^{(p+2,p+1)}$ can be written as

$$D_i^{(p+2,p+1)} \approx |\langle \mathbf{g}_{p+2}, \mathbf{g}_p \rangle| \tau(\omega) |G_{(p+2,i)}| (e^{j\alpha_{(p+2,p)}} e^{j\theta_{(p+2,i)}} - e^{j\alpha_{(p+1,p)}} e^{j\theta_{(p+1,i)}}) \quad (14)$$

Note that the clutter components canceled out upon subtraction and this is one of the important advantages of differential processing. After some phase manipulation, the above equation can be written as

$$D_i^{(p+2,p+1)} \approx |\langle \mathbf{g}_{p+2}, \mathbf{g}_p \rangle| \tau(\omega) |G_{(p+2,i)}| e^{j\frac{\alpha_{(p+2,p)}}{2}} e^{j\frac{\alpha_{(p+1,p)}}{2}} e^{j\frac{(\theta_{(p+2,i)} + \theta_{(p+1,i)})}{2}} \times 2j \sin\left(\frac{\alpha_{(p+2,p)} - \alpha_{(p+1,p)}}{2} + \frac{\theta_{(p+2,i)} - \theta_{(p+1,i)}}{2}\right) \quad (15)$$

As we saw in Section 3.1.1, $\tau(\omega)$ has, in general, nonlinear phase response with frequency. Further processing can be done to eliminate its unknown phase whereby the differential vector $\mathbf{d}^{(p+2,p+1)}$ is normalized by the inner product between $\mathbf{d}^{(p+2,p+1)}$ itself and \mathbf{g}_p . In this way, the phase of the i^{th} component of $\mathbf{d}^{(p+2,p+1)}$ becomes

$$-\frac{\alpha_{(p+2,p)}}{2} - \frac{\alpha_{(p+1,p)}}{2} + \frac{\theta_{(p+2,i)} + \theta_{(p+1,i)}}{2} \quad (16)$$

where $\Phi_{\tau(\omega)}$ is absent.

Finally, to detect the target's new location, $\mathbf{d}^{(p+2,p+1)}$ is projected onto the imaging domain. The projection at location I in the imaging domain is given by

$$P_I = \left\langle \frac{\mathbf{g}_I}{\|\mathbf{g}_I\|}, \frac{\mathbf{d}^{(p+2,p+1)}}{\|\mathbf{d}^{(p+2,p+1)}\|} \right\rangle \quad (17)$$

A similar expression can be written for P_I as in (7), where the phase of the i^{th} term is given by

$$\Phi_{P_{(I,i)}} = \frac{\alpha_{(p+2,p)}}{2} + \frac{\alpha_{(p+1,p)}}{2} - \frac{\theta_{(p+2,i)} + \theta_{(p+1,i)}}{2} + \theta_{(I,i)} \quad (18)$$

To verify the approach, differential processing is applied to track a target moving in homogeneous background. Actual and detected traces are shown in Fig. 9(b). Consider the projection at each of the following locations indicated in Fig. 9(b). Note that, without loss of generality, it is assumed that the initial target's location p coincides with location $p+1$ as shown in the figure.

(a) Location $p+1$:

$$\theta_{(I,i)} = \theta_{(p+1,i)} \quad (19)$$

From (18), $\Phi_{P_{(p+1,i)}}$ becomes

$$\Phi_{P_{(p+1,i)}} = \frac{\alpha_{(p+2,p)}}{2} + \frac{\alpha_{(p+1,p)}}{2} - \frac{\theta_{(p+2,i)} - \theta_{(p+1,i)}}{2} \quad (20)$$

which has $-(\theta_{(p+2,i)} - \theta_{(p+1,i)})/2$ variation with i as shown in Fig. 11.

(b) Location $p+2$:

$$\theta_{(I,i)} = \theta_{(p+2,i)} \quad (21)$$

and from (18), $\Phi_{P_{(p+2,i)}}$ is given by

$$\Phi_{P_{(p+2,i)}} = \frac{\alpha_{(p+2,p)}}{2} + \frac{\alpha_{(p+1,p)}}{2} + \frac{\theta_{(p+2,i)} - \theta_{(p+1,i)}}{2} \quad (22)$$

which has $(\theta_{(p+2,i)} - \theta_{(p+1,i)})/2$ variation with i as shown in Fig. 11.

(c) Focusing location:

Assume that a location I exists such that

$$\theta_{(I,i)} = \frac{\theta_{(p+2,i)} + \theta_{(p+1,i)}}{2} \quad (23)$$

then, from (18), $\Phi_{P_{(I,i)}}$ is given by

$$\Phi_{P_{(I,i)}} = \frac{\alpha_{(p+2,p)}}{2} + \frac{\alpha_{(p+1,p)}}{2} \quad (24)$$

which is independent of i , i.e. all components of the inner product of P_I add in phase. We call this location the ‘‘focusing location’’. At the focusing location, $|P_I|$ assumes a maximum value of

$$|P_I| = \left| \sum_{i=1}^N \frac{|G_{(I,i)}|}{\|\mathbf{g}_I\|} \frac{u_i}{\|\mathbf{u}\|} \right| \quad (25)$$

where

$$u_i = \sin \left(\frac{\alpha_{(p+2,p)} - \alpha_{(p+1,p)}}{2} + \frac{\theta_{(p+2,i)} - \theta_{(p+1,i)}}{2} \right) |G_{(p+2,i)}| \quad (26)$$

is the i^{th} component of \mathbf{u} . However, there is no guarantee that there exists a location satisfying the focusing condition (23) for all frequencies. So it would be more accurate to determine the focusing location by considering the projection in the time domain $P_I(t)$, obtained by taking the inverse Fourier transform of the projection in the frequency domain. The location at which $P_I(t)$ peaks is the one that best satisfies (23) over the bandwidth of interest. Note that the time instant at which the peak of $P_I(t)$ occurs is irrelevant to determining the focusing location, and is determined by the phase of P_I shown in Fig. 12(b).

Focusing (detected) locations in Fig. 9(b) are determined using the projection in the time-domain as described above. The detected locations lie somewhere in between locations $p + 1$ and $p + 2$ as expected from the ideal focusing condition (23). Fig. 11 shows that the components of the inner product of P_I at the focusing location are almost in phase, which agrees well with our assumption.

The magnitude of the projections at the above three locations are shown in Fig. 12(a). It is clear that the focusing location has the maximum projection over the entire bandwidth. Note also that this maximum is close to one as long as $\sin \left(\frac{\alpha_{(p+2,p)} - \alpha_{(p+1,p)}}{2} + \frac{\theta_{(p+2,i)} - \theta_{(p+1,i)}}{2} \right)$ varies only slightly with i , as can be seen from (25) and (26).

Determining the focusing location from the time-domain projection is also useful in case of incoherent projection, where the frequency components have random phase relationship among them. This situation occurs in the case of tracking under the presence of clutter, where different frequency components ‘‘respond’’ to the clutter differently. More discussion on this is presented in Section 3.3.

3.1.3. Traceability

In this subsection we discuss the effect of the operating frequency on the ability of the differential tracking algorithm to track small motions of the target. This characterizes the sensitivity of the algorithm. The ability of the algorithm to detect (focus on) the new location rather than the prior location depends on how large the projection at the focusing location (which is biased towards the new location) is compared with that at the prior location. In other words, the more ‘‘defocused’’ the projection at the prior location is, the more sensitive the algorithm will respond to the motion.

As discussed in the last subsection, the phases of the constituting terms of the projection on location $p+1$ ($\Phi_{P_{(p+1,i)}}$) vary with i as $-(\theta_{(p+2,i)} - \theta_{(p+1,i)})/2$. So the

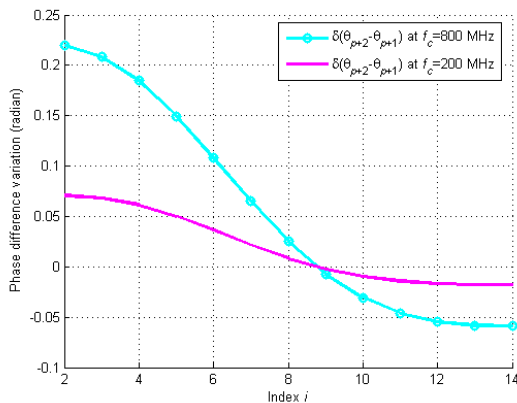


Figure 13. Variation of $\theta_{(p+2,i)} - \theta_{(p+1,i)}$ from one array element to the other for the two frequency bands indicated in Fig. 12(a).

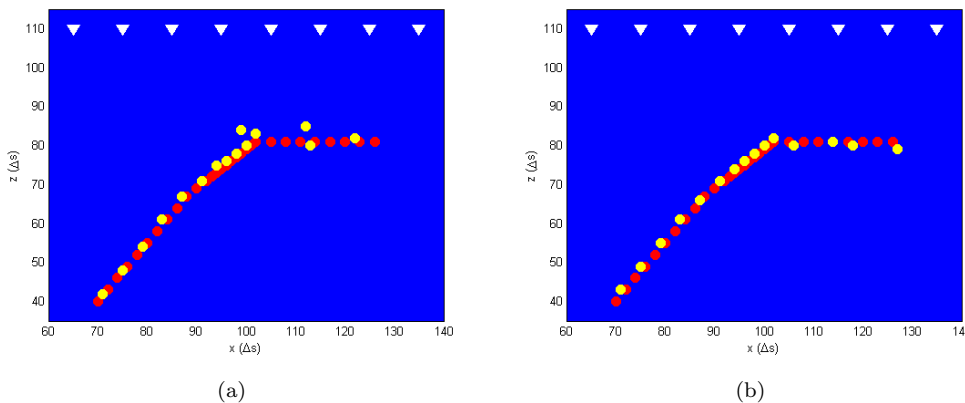


Figure 14. Actual (red) and detected (yellow) traces for (a) the lower frequency band. (b) the upper frequency band. Higher center frequency results in better tracking sensitivity. The array elements are indicated by white triangles.

larger the variation of $(\theta_{(p+2,i)} - \theta_{(p+1,i)})$ with i , the more defocused the projection will be at location $p + 1$. The variation of $(\theta_{(p+2,i)} - \theta_{(p+1,i)})$ with respect to the antenna index i for the two highlighted lower and upper frequency bands in Fig. 12(a), are shown in Fig. 13. This figure shows that, as the center frequency f_c increases, the phase difference variation increases and the algorithm becomes more sensitive to the movement. Note that a similar feature is presented by Doppler radars. Detected traces corresponding to the aforementioned frequency bands are shown in Fig. 14. It is apparent that the detected movement trace utilizing higher f_c agrees better with the actual movement trace.

3.2. Performance in clutter

In this section, we present simulation results of the differential tracking algorithm applied to moving target in discrete clutter (secondary scatterers). The setup is shown in Fig. 15. A point-like metallic target is moving (towards the antenna array location) in a room enclosed by four walls with $\epsilon_r = 8$ and in the presence of four other secondary discrete scatterers, e.g. pillars. All pillars have $\epsilon_r = 14$. Fig. 15(a) shows the actual and detected traces when the synthesized imaging domain used for backprojection takes the clutter into account (that is, the Green's function used for the inverse problem (backprojection) incorporates the presence of the walls and the pillars). Very good agreement between the actual and the constructed traces

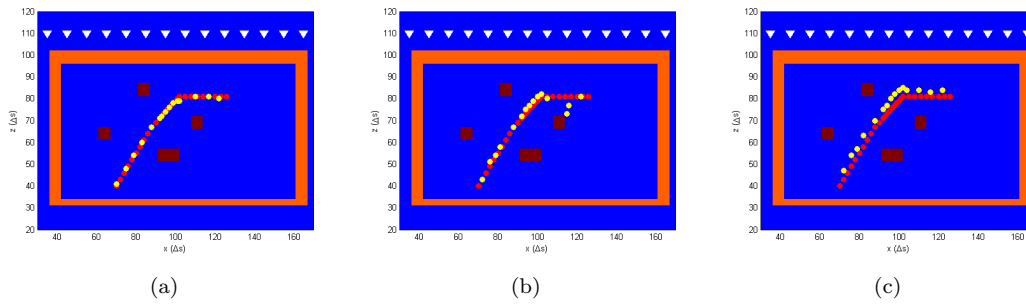


Figure 15. Performance of differential tracking in discrete clutter. Actual trace (red) and detected traces (yellow). Moving target is surrounded by four walls ($\epsilon_r = 8$) and in the presence of four pillars ($\epsilon_r = 14$) (a) Imaging domain takes into account the walls and the pillars. (b) Imaging domain takes into account the front wall only. (c) Imaging domain is a homogeneous medium. The array elements are indicated by white triangles. The wall thickness is purposely different for the front-, lateral-, and back-walls

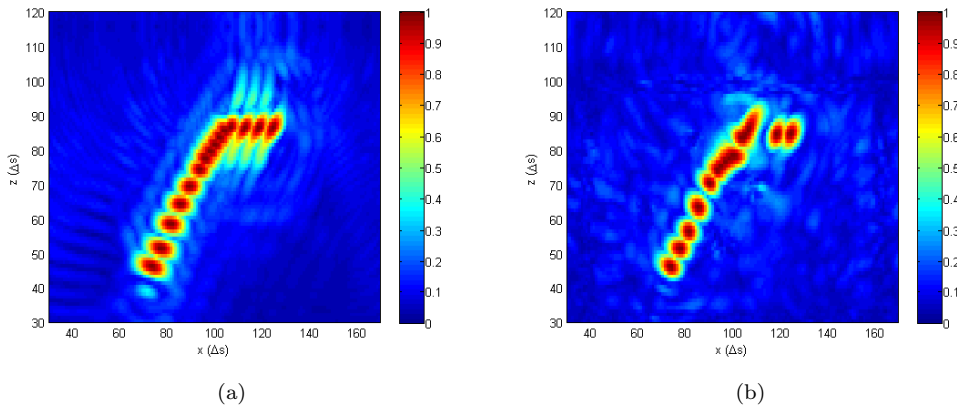


Figure 16. Moving target's images along its trace. (a) The target is moving in homogeneous background. (b) The target is moving in the presence of discrete clutter.

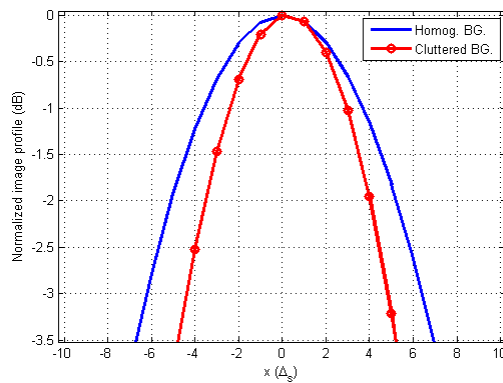


Figure 17. Normalized cross-range profiles of the images at the lowermost location of the target.

is achieved. Information about the location, size, and composition of the point-like stationary scatterers can be provided by the discrimination algorithm explained in the first part of the paper.

Fig. 15(b) shows the performance when only the front wall properties are known to the inverse problem. Some deviations in tracking occur due to the unaccounted-for multipath in the utilized (estimated) Green's function. Finally, Fig. 15(c) shows the performance when backprojection occurs on homogeneous medium, that is, when the utilized Green's function does not incorporate any secondary scatterers. The algorithm is still capable of tracking the motion well. However, the detected

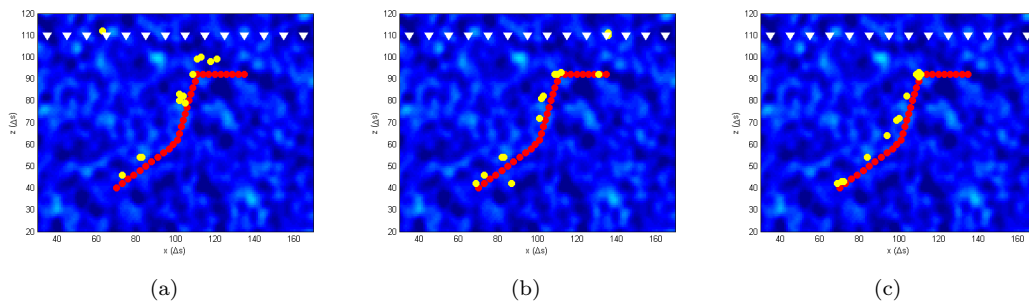


Figure 18. Performance of differential tracking in continuous random clutter: bandwidth effect. A different random medium realization is used for backprojection. A center frequency of 507 MHz is used with different bandwidths. (a) Bandwidth = 253 MHz, average deviation = $16.8\Delta_s$. (b) Bandwidth = 507 MHz, average deviation = $8.5\Delta_s$. (c) Bandwidth = 760 MHz, average deviation = $9\Delta_s$.

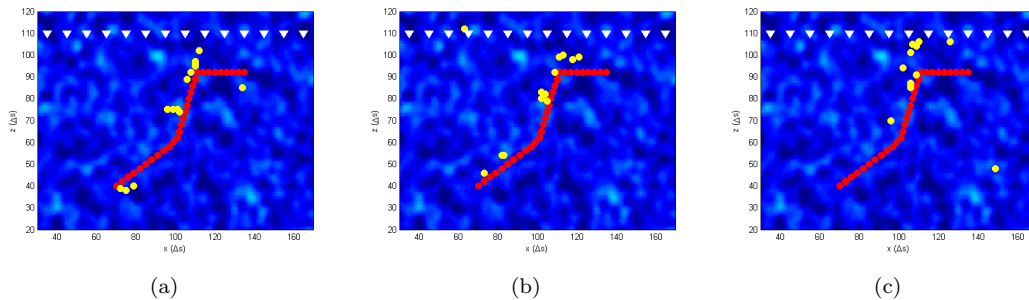


Figure 19. Performance of differential tracking in continuous random clutter; center frequency effect. A different random medium realization is used for backprojection. A bandwidth of 253 MHz is used with different center frequencies. (a) $f_c = 253$ MHz, average deviation = $11.4\Delta_s$. (b) $f_c = 507$ MHz, average deviation = $16.8\Delta_s$. (c) $f_c = 760$ MHz, average deviation = $28.6\Delta_s$.

trace is slightly shifted upwards due to the (unaccounted) delay caused by the front wall permittivity.

Images of the moving target at different locations along its trace are shown in Fig. 16. Fig. 16(a) shows the images when the target is moving in a homogeneous medium, whereas Fig. 16(b) shows the images when the same target is moving in the presence of four walls and four pillars as depicted in Fig. 15. It can be noticed that the images in the presence of clutter are more focused along the cross-range direction than in the absence of clutter; this is the *superresolution* effect offered by TR [17, 20]. The cross-range resolution is proportional to $\lambda L/a_e$, where L is the distance between the target and the array and a_e is the *effective* aperture of the array [45]. The normalized cross-range profiles of the images at the first (lowermost) location are plotted in Fig. 17. A reduction of about 30% in the half maximum width is achieved in the presence of clutter. This means that the multipath offered by the clutter effectively increased the antenna aperture by approximately 30% in this particular example. We can also notice, in Fig. 16, successive improvement in the resolution as the target moves closer to the array, as expected.

3.3. Statistical stability

Statistical stability is another distinctive feature of UWB TR techniques. Under certain conditions, different frequency components of the interrogating signal “perceive” the random medium differently than other (sufficiently well separated) frequency components. This implies a “frequency averaging” effect that mimics an ensemble averaging, making the image independent of the particular random medium realization and instead depending only on the medium *statistics* [22, 25]. In this section, we examine the statistical stability of the tracking algorithm as a function

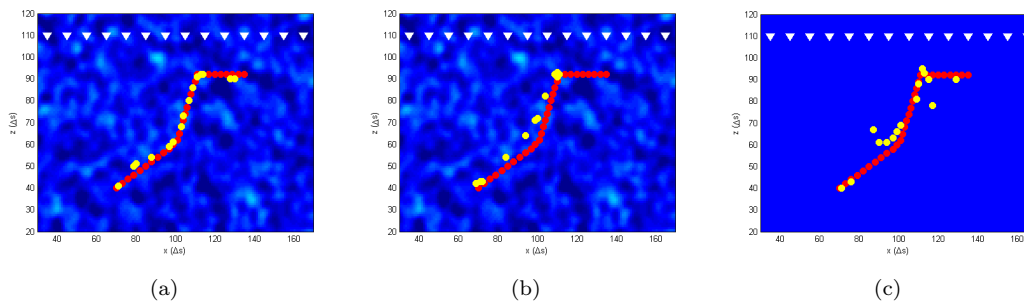


Figure 20. Performance of differential tracking in continuous random clutter; background effect. $f_c = 507$ MHz and bandwidth = 760 MHz with different imaging backgrounds. (a) Imaging in the same random realization, average deviation = $3.38\Delta_s$. (b) Imaging in a different random realization, average deviation = $9\Delta_s$. (c) Imaging in homogeneous medium, average deviation = $6.3\Delta_s$.

of the bandwidth, the center frequency of operation, and the background medium properties. In this context, we quantify statistical stability by the average deviation in the detected trace from the actual one; that is, the less the deviation, the more stable the tracking is.

In this case, the background is assumed as a realization of a continuous random medium with permittivity fluctuations following a clipped Gaussian distribution with mean permittivity $\epsilon_{rm} = 2$, standard deviation $\sigma = 0.3\epsilon_{rm}$ and correlation length $l_c = 10\Delta_s$, $\Delta_s = 2.5$ cm [51, 52]. A different realization having the same statistical properties is used for backprojection. The bandwidth effect is examined in Fig. 18, where traces constructed using successively increasing bandwidths are plotted. It is obvious from this figure that as the bandwidth increases, the tracing quality is improved.

The center frequency effect is considered in Fig. 19. Traces obtained using increasingly higher center frequencies (while maintaining constant bandwidth) are shown. It can be noticed that as the center frequency decreases, the trace becomes more stable. This is because of the fact that as the wavelength increases with respect to the correlation length, the random medium behaves more like an effectively homogeneous medium. Note that the effect of increasing the center frequency on statistical stability counteracts its effect on tracking sensitivity. A compromise has to be made to select the optimum operating frequency given the expected medium statistics.

Finally, for a given bandwidth and center frequency the effect of backprojecting on different media is considered in Fig. 20. In Fig. 20(a) the exact random realization is assumed to be known and used for projection. Perfect tracking is obtained, as expected. In Fig. 20(b) and (c) a different realization with the same properties and a homogeneous medium are used, respectively, for projection. Comparable tracking is obtained in both cases, with part (b) performing better in the first part of the trace but getting stuck at some point. A more comprehensive study incorporating all factors affecting statistical stability is under development and will be presented elsewhere.

3.4. Multiple targets tracking

The performance of the algorithm when used to track multiple targets is examined in this section. As mentioned before, the algorithm is fed with the initial locations of each of the moving targets and starts transmitting focused beams (which are the time-reversed steering vectors of the targets' locations) alternatively to each of those locations. Differential processing is applied to determine the updated location of each target and the process is repeated. Fig. 21(a) shows the case of tracking

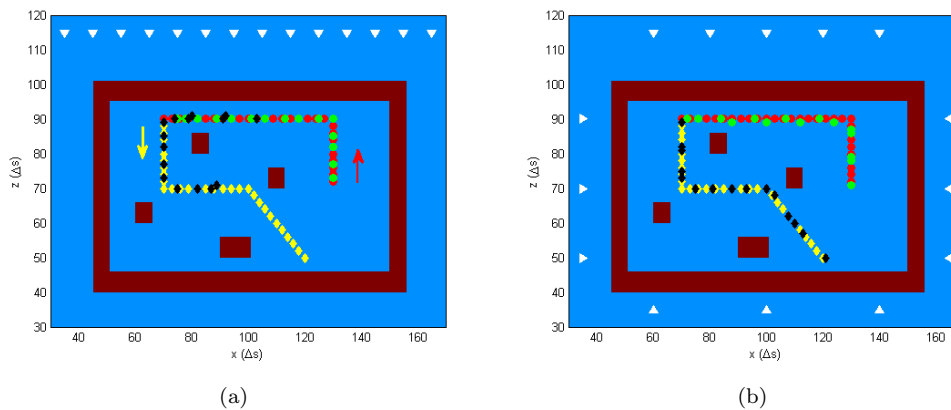


Figure 21. Two-targets tracking with non-intersecting paths. Red and green dots respectively indicate actual and detected traces of the first target moving upwards. Yellow and black diamonds respectively indicate actual and detected traces of the second target moving downwards. Four stationary targets (pillars) are present and the entire domain is surrounded by walls. Array elements are indicated by white triangles. (a) Linear 14-elements antenna array. (b) Full aspect 14-elements array.

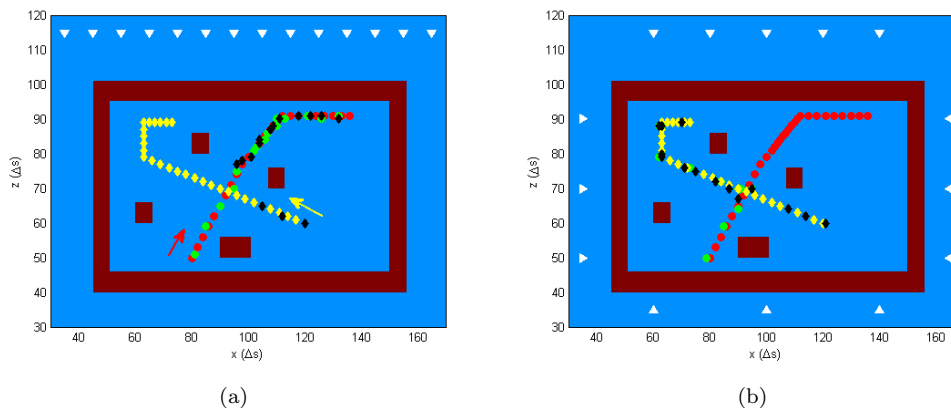


Figure 22. Two-targets tracking with intersecting paths. Red and green dots respectively indicate actual and detected traces of the first target moving to the right. Yellow and black diamonds respectively indicate actual and detected traces of the second target moving to the left. Array elements are indicated by white triangles. (a) Linear 14-elements antenna array. (b) Full aspect 14-elements array.

two targets using a linear 14-elements array. Tracking is successful as long as the targets do not cross through the wave paths between the array and other targets. When the latter situation occurs, ambiguity ensues; both beams start tracking the dominant (e.g. closer) target to the array. This ambiguity can be mitigated, for example, by using a full aspect array as shown in Fig. 21(b). A full aspect array guarantees the presence of uninterrupted wave paths between each target and at least some of the array elements.

Another situation is shown in Fig. 22, where the traces of the two moving targets intersect. At this point, the two focused beams will be pointing to the same location, hence there will be no guarantee that the beams will continue on tracking their respective targets. The beams may be swapped or both of them can track one and the same target resulting in the loss of tracking of the other, as shown in the Fig 22(a). Even the use of a full aspect array does not resolve the ambiguity in this case, as shown in Fig. 22(b). It becomes necessary to record MDMs of two snapshots and apply DORT on the differential MDM to determine the new locations of the targets.

4. Conclusion

Two algorithms for identifying and tracking moving targets in clutter based on TR techniques have been developed. The first algorithm classifies targets into stationary and moving ones by applying the DORT to the averaged and differential MDMs acquired at consecutive time instants. The number of stationary and moving targets, as well as their locations and images can be determined. Moreover, electrical lengths of dielectric targets can be estimated from their eigenspectra. The second algorithm provides real-time tracking of moving targets using differential TR processing. The performance of the algorithm in the presence of discrete and continuous random clutter is evaluated. It was shown to have outstanding clutter rejection performance thanks to differential processing. The algorithm is capable of tracking multiple targets as long as their paths do not intersect. The tracking algorithm is an efficient algorithm in terms of processing time and memory resources. It also utilizes selective beams focused at each moving target rather than illuminating the entire domain; this suggests possible applications in communication covertness for example.

Acknowledgement

This work has been supported by the National Science Foundation (NSF) under grant EECS-0925272 and by the Ohio Supercomputing Center (OSC) under grant PAS-0110.

References

- [1] E.J. Baranoski, *Through-wall imaging: Historical perspective and future directions*, Journal of the Franklin Institute 345 (2008), pp. 556–569.
- [2] A.M. Attiya, A. Bayram, A. Safaai-Jazi, and S.M. Riad, *UWB applications for through-wall detection*, in Proc. IEEE Antennas Propag. Int. Symp. 3 (2004), pp. 3079–3082.
- [3] L. Borcea, G. Papanicolaou, and C. Tsogka, *Theory and applications of time reversal and interferometric imaging*, Inverse Prob. 19 (2003), pp. 1–26.
- [4] ———, *Interferometric array imaging in clutter*, Inverse Prob. 21 (2005), pp. 1419–1460.
- [5] J.M.F. Moura and Y.W. Jin, *Time reversal imaging by adaptive interference canceling*, IEEE Trans. Signal Process. 56 (2008), pp. 233–247.
- [6] D. Liu, G. Kang, L. Li, Y. Chen, S. Vasudevan, W. Joines, Q.H. Liu, J. Krolik, and L. Carin, *Electromagnetic time-reversal imaging of a target in a cluttered environment*, IEEE Transactions on Antennas and Propagation 53 (2005), pp. 3058–3066.
- [7] M. Fink, *Time reversal mirrors*, J. Phys. D.: Appl. Phys. 26 (1993), pp. 1333–1350.
- [8] M. Fink, D. Cassereau, A. Derode, C. Prada, P. Roux, M. Tanter, J. Thomas, and F. Wu, *Time reversed acoustics*, Rep. Prog. Phys. 63 (2000), pp. 1933–1995.
- [9] G. Micolau and M. Saillard, *DORT method as applied to electromagnetic subsurface sensing*, Radio Sci. 38 (2003), pp. 1038–1049.
- [10] G. Lerosey, J. de Rosny, A. Tourin, A. Derode, G. Montaldo, and M. Fink, *Time reversal of electromagnetic waves*, Phys. Rev. Lett. 92 (2004).
- [11] F.D. Philippe, C. Prada, J. de Rosny, D. Clorennec, J.G. Minonzio, and M. Fink, *Characterization of an elastic target in a shallow water waveguide by decomposition of the time-reversal operator*, J. Acoust. Soc. Am. 124 (2008), pp. 779–787.
- [12] M.E. Yavuz and F.L. Teixeira, *Space-frequency ultrawideband time-reversal imaging*, IEEE Trans. Geosci. Remote Sensing 46 (2008), pp. 1115–1124.
- [13] M.S. L. Bellomo S. Pioch and E. Spano, *Time reversal experiments in the microwave range: Description of the radar and results*, Prog. Electromagnetics Research 104 (2010), pp. 427–448.
- [14] M.E. Yavuz and F.L. Teixeira, *On the sensitivity of time-reversal imaging techniques to model perturbations*, IEEE Trans. Antennas Propagat. 56 (2008), pp. 834–843.
- [15] ———, *Frequency dispersion in time reversal techniques for UWB electromagnetic waves*, IEEE Geosci. Remote Sens. Lett. 2 (2005), pp. 233–237.
- [16] G. Lerosey, J. de Rosny, A. Tourin, and M. Fink, *Focusing beyond the diffraction limit with far-field time reversal*, Science 315 (2007), pp. 1120–1122.
- [17] A. Devaney, *Super-resolution processing of multistatic data using time reversal and MUSIC*, (Accessed in Nov. 2009), Unpublished paper, preprint available on the authors web site. Available Online: <http://www.ece.neu.edu/faculty/devaney/>.

- [18] M.E. Yavuz and F.L. Teixeira, *A numerical study of time reversed UWB electromagnetic waves in continuous random media*, IEEE Antennas Wirel. Prop. Lett. 4 (2005), pp. 43–46.
- [19] S.K. Lehman and A.J. Devaney, *Transmission mode time-reversal super-resolution imaging*, Acoustical Society of America Journal 113 (2003), pp. 2742–2753.
- [20] P. Blomgren, G. Papanicolaou, C. Tsogka, and J. Berryman, *Super resolution in time-reversal acoustics*, J. Acoust. Soc. Am. 111 (2002), pp. 230–248.
- [21] J.G. Berryman, L. Borcea, G. Papanicolaou, and C. Tsogka, *Statistically stable ultrasonic imaging in random media*, J. Acoust. Soc. Am. 112 (2002), pp. 1509–1522.
- [22] G. Papanicolaou, L. Ryzhik, and K. Solna, *Statistical stability in time reversal*, SIAM J. Appl. Math. 64 (2004), pp. 1133–55.
- [23] L. Borcea, G. Papanicolaou, C. Tsogka, and J. Berryman, *Imaging and time reversal in random media*, Inverse Prob. 18 (2002), pp. 1247–1279.
- [24] M.E. Yavuz and F.L. Teixeira, *Full time-domain DORT for ultrawideband fields in dispersive, random inhomogeneous media*, IEEE Trans. Antennas Propagat. 54 (2006), pp. 2305–2315.
- [25] A. Derode, A. Tourin, and M. Fink, *Random multiple scattering of ultrasound. II. Is time reversal a self-averaging process?*, Phys. Rev. 64 (2001).
- [26] M. Skolnik *Introduction to Radar Systems*, 3rd McGraw-Hill, NY, 2001.
- [27] S.S. Ram and H. Ling, *Through-wall tracking of human movers using joint Doppler and array processing*, IEEE Geosci. Remote Sens. Lett. 5 (2008), pp. 537–541.
- [28] T. Gibson and J. Jenn, *Prediction and measurement of wall insertion loss*, IEEE Trans. Antennas Propagat. 47 (1999), pp. 55–57.
- [29] S. Nag, H. Fluhler, and M. Barnes, *Preliminary interferometric images of moving targets obtained using a time-modulated ultrawide band through-wall penetration radar*, in *Proceedings of the 2001 IEEE Radar Conference*, Atlanta, Georgia, 2001.
- [30] S. Nag, M. Barnes, T. Payment, and G. Holladay, *Ultrawideband through-wall radar for detecting the motion of people in real time*, SPIE Proceedings of the Radar Sensor Technology and Data Visualization 4744 (2002), pp. 48–57.
- [31] S. Nag and M. Barnes, *A moving target detection filter for an ultra-wideband radar*, in *Proceedings of the 2003 IEEE Radar Conference*, Huntsville, Alabama, 2003, pp. 147–153.
- [32] W. Zheng, Z. Zhao, and Z.P. Nie, *Application of TRM in the UWB through wall radar*, Prog. Electromagnetics Res. PIER 87 (2008), pp. 279–296.
- [33] M.E. Yavuz, *Through-the-wall sensing using time-reversal antenna array*, in *EUCAP10-European Conference on Antennas and Propagation*, Barcelona, Spain, 2010.
- [34] N. Maaref, P. Millot, and X. Ferrieres, *Electromagnetic imaging method based on time reversal processing applied to through-the-wall target localization*, Progress in Electromagnetics Research M 1 (2008), pp. 59–67.
- [35] E.A. Marengo, F.K. Gruber, and F. Simonetti, *Time-reversal MUSIC imaging of extended targets*, IEEE Trans. Image Processing 16 (2007), pp. 1967–1984.
- [36] H. Zhao, *Analysis of the response matrix for an extended target*, SIAM J. Appl. Math. 64 (2004), pp. 725–745.
- [37] S. Hou, K. Solna, and H. Zhao, *Imaging of location and geometry for extended targets using the response matrix*, J. Comp. Phys. 199 (2004), pp. 317–338.
- [38] H.T. Nguyen, J.B. Andersen, G.F. Pedersen, P. Kyritsi, and P.C.F. Eggers, *Time reversal in wireless communications: A measurement-based investigation*, IEEE Trans. Wireless Comm. 5 (2006), pp. 2242–2252.
- [39] G. Montaldo, G. Lerosey, A. Derode, A. Tourin, J. de Rosny, and M. Fink, *Telecommunication in a disordered environment with iterative time reversal*, Waves in Random Media 14 (2004), pp. 287–302.
- [40] S.S. Ram, Y. Li, A. Lin, and H. Ling, *Doppler-based detection and tracking of humans in indoor environments*, Journal of the Franklin Institute 345 (2008), pp. 679–699.
- [41] A. Taflov and S. Hagness *Computational Electrodynamics: The Finite-Difference Time-Domain Method*, 3rd Artech House, Norwood, MA, 2005.
- [42] J.P. Berenger, *A perfectly matched layer for the absorption of electromagnetic waves*, J. Comput. Phys. 114 (1994), pp. 185–200.
- [43] F.L. Teixeira and W.C. Chew, *A general approach to extended Berenger’s absorbing boundary condition to anisotropic and dispersive media*, IEEE Trans. Antennas Propagat. 46 (1998), pp. 1386–1387.
- [44] A.J. Devaney, *Time reversal imaging of obscured targets from multistatic data*, IEEE Transactions on Antennas and Propagation 53 (2005), pp. 1600–1610.
- [45] M.E. Yavuz and F.L. Teixeira, *Ultrawideband microwave sensing and imaging using time-reversal techniques: A review*, Remote Sens. 9 (2009), pp. 466–495.
- [46] F.J. Harris, *On the use of windows for harmonic analysis with the discrete Fourier transform*, Proc. IEEE 66 (1978), pp. 51–83.
- [47] C. Prada and M. Fink, *Eigenmodes of the time reversal operator: A solution to selective focusing in multiple-target media*, Wave Motion 20 (1994), pp. 151–163.
- [48] C. Prada, S. Manneville, D. Spoliansky, and M. Fink, *Decomposition of the time reversal operator: Detection and selective focusing on two scatterers*, J. Acoust. Soc. Am. 99 (1996), pp. 2067–2076.
- [49] H. Torteil, G. Micolau, and M. Saillard, *Decomposition of the time reversal operator for electromagnetic scattering*, J. Electromagn. Waves Appl. 13 (1999), pp. 687–719.
- [50] G. Micolau, M. Saillard, and P. Borderies, *DORT method as applied to ultrawideband signals for detection of buried objects*, IEEE Trans. Geosci. Remote Sens. 41 (2003), pp. 1813–1820.
- [51] F.L. Teixeira, W.C. Chew, M. Straka, M.L. Oristaglio, and T. Wang, *Finite-difference time-domain simulation of ground penetrating radar on dispersive, inhomogeneous and conductive soils*, IEEE-Trans. Geosci. Remote Sensing 36 (1998), pp. 1928–1937.
- [52] C.D. Moss, F.L. Teixeira, Y.E. Yang, and J.A. Kong, *Finite-difference time-domain simulation of scattering from objects in continuous random media*, IEEE Trans. Geosci. Remote Sens. 40 (2002), pp. 178–186.

Appendix A. On some heuristics for target characterization using DORT

In this appendix, we present some heuristics for characterization of scatterers using the eigenvalue/vector decomposition provided by the DORT. Using this information, we can determine the composition of the scatterer being either metallic or dielectric, and plot the image of the scatterer showing its cross-range extension. We can also estimate the co-range electrical length in case of dielectric scatterers.

We start by explaining the approach, followed by a presentation of results for different metallic and dielectric targets.

A.1. Approach

The MDM of a point-like scatterer, located at point p , has *one* significant singular value/vector. The singular value of the MDM (which equals the square root of the eigenvalue of the corresponding TRO) at frequency ω is given by

$$\mu(\omega) = |s(\omega)| |\tau(\omega)| \|\mathbf{g}_p\|^2 \quad (\text{A1})$$

where $s(\omega)$ is the spectrum of the input pulse and $\tau(\omega)$ is the target's scattering coefficient. The singular vector (which equals the eigenvector of the corresponding TRO) is given by

$$\mathbf{v}(\omega) = \frac{\mathbf{g}_p^*}{\|\mathbf{g}_p\|} \quad (\text{A2})$$

So, in principle, singular values carry information on the scattering coefficients as functions of frequency and singular vectors carry information on the locations of the targets.

The singular value spectrum can be used to determine whether the target is metallic or dielectric. Metallic targets, with sufficiently high conductivity, have almost “flat” scattering coefficient spectrum in the frequency band of interest (microwave range assumed here). On the other hand, dielectric targets act as imperfect resonators. So their singular values spectra have periodic “peaks” and “valleys” corresponding to constructive and destructive interferences. The first valley frequency f_v can be approximately described by the 1-D resonator relation

$$f_v = \frac{f_c \lambda}{2l_z} \quad (\text{A3})$$

where f_c is the operating frequency, λ is the wavelength inside the dielectric target and l_z is the dimension of the target along the co-range direction.

For a given operating frequency, f_v depends only on the electrical length of the target. Thus, valley frequencies can be used to estimate the co-range electrical length of the target.

Extended targets across the co-range are also associated with *one* significant singular value/vector. The image of the singular vector corresponds to the side of the target facing the array. The co-range extension can be estimated through the singular value spectrum as described before.

Extended targets across the cross-range are associated with *multiple* significant singular values depending on their size. If the composition of the target is uniform, all these singular values have similar spectrum. The associated singular vectors point to different scattering centers on the target. Therefore, to estimate the

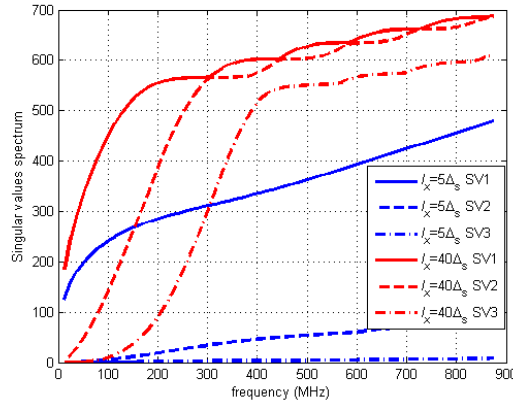


Figure A1. Spectra of the first three singular values (SVs) of two metallic targets. The singular values are normalized with respect to the input pulse spectrum.

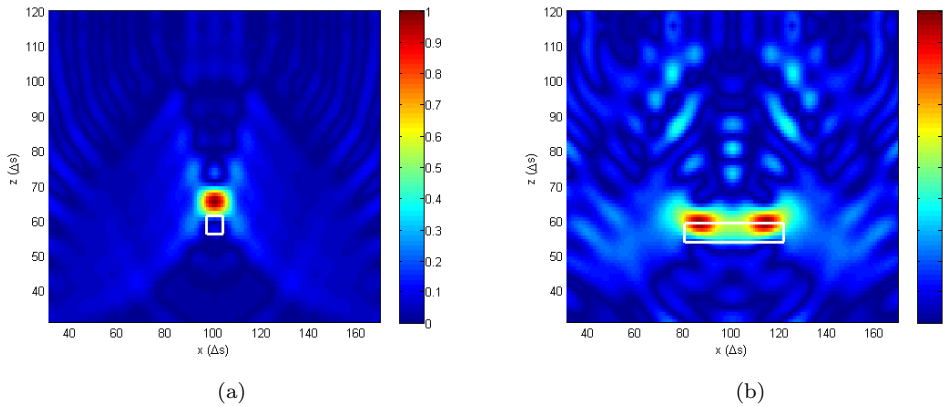


Figure A2. Images of the sum of the significant singular vectors of metallic targets: (a) point-like target ($l_x = 5\Delta_s$). (b) extended target ($l_x = 40\Delta_s$). The actual targets are indicated by white rectangles.

cross-range extension, we can, for example, construct the image of the *sum* of the significant singular vectors weighted by the respective singular values.

A.2. Simulation results

A.2.1. Metallic targets

The spectra of the first (most significant) three singular values of two metallic targets are shown in Fig. A1. The first target is point-like with $l_x = 5\Delta_s$ and $l_z = 5\Delta_s$, $\Delta_s = 2.5$ cm. The second target is extended along the cross-range direction with $l_x = 40\Delta_s$ and $l_z = 5\Delta_s$. The singular values are normalized with respect to the input pulse spectrum, so that the plotted spectra directly express the targets' scattering coefficients.

It can be noticed that the point-like target has only one significant singular value, whereas, the extended target has three significant values (those that have comparable magnitudes). Also, we can notice that, all significant singular values have similar spectra. This spectrum is almost flat with frequency with some linear dependence because of the $\|\mathbf{g}_p\|^2$ factor in μ .

The image of the significant singular vector for the point-like target is shown in Fig. A2(a), and the image of the sum of the three singular vectors of the extended target is shown in Fig. A2(b). Both images indicate the shape of the corresponding targets reasonably well. Of course, for an extended target, the image of the sum of

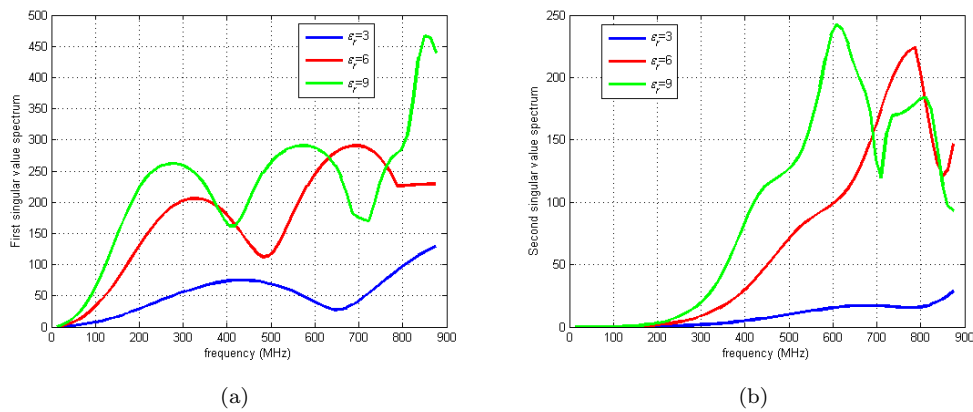


Figure A3. Singular values spectra of point-like dielectric targets with different permittivities. (a) First singular values. (b) Second singular values.

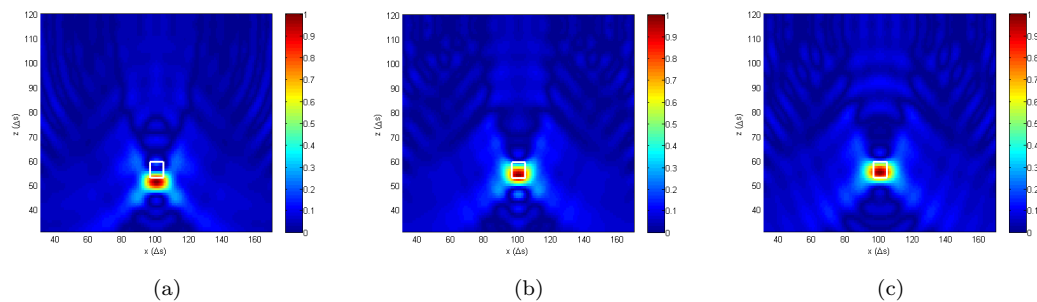


Figure A4. Images of the first singular vectors of dielectric targets with different permittivities. (a) $\epsilon_r = 3$. (b) $\epsilon_r = 6$. (c) $\epsilon_r = 9$. The actual targets are indicated by white rectangles.

Table A1. Actual and estimated electrical lengths of point-like dielectric targets with different permittivities

ϵ_r	3	6	9
actual l_z/λ	0.29	0.408	0.5
estimated l_z/λ	0.307	0.412	0.49
% error	5.8	0.9	2

the significant singular vectors is more indicative of the target's shape than those of any individual singular vectors.

A.2.2. Dielectric targets

(a) Permittivity effect:

Fig. A3(a) and (b) show the spectra of the first and second singular values, respectively, of three near point-like dielectric targets with different permittivities. The targets' sizes are $5\Delta_s \times 5\Delta_s$ and have relative permittivities $\epsilon_r = 3, 6$ and 9 . We can see that the spectra of the first singular values have the peaks/valleys response of dielectric resonators. The valleys frequencies are used to estimate the electrical sizes of the targets along the co-range direction. Actual and estimated electrical lengths are summarized in Table A1. Very accurate estimation is achieved. The second singular values do not possess the same spectra as those of the first. This indicates that each target is associated with only one significant value; this is expected since they are near point-like targets.

The images of the first singular vectors are shown in Fig. A4, expressing the targets shapes well.

(b) Co-range extension effect:

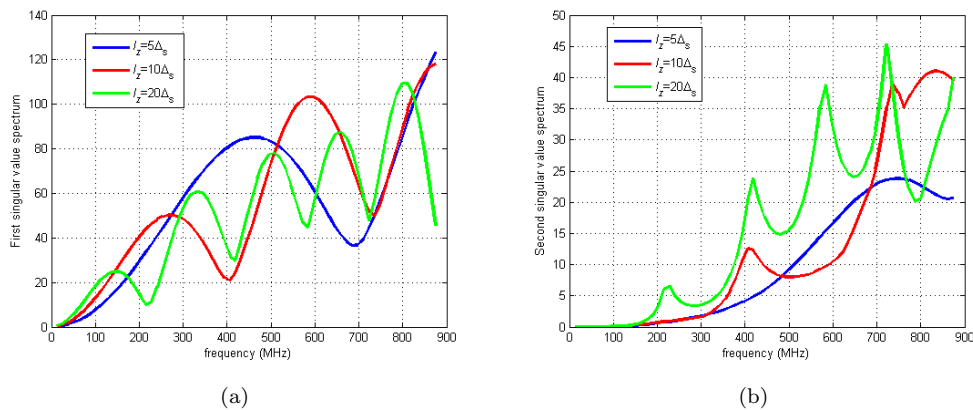


Figure A5. Singular values spectra of co-range extended dielectric targets with similar permittivities. (a) First singular values. (b) Second singular values.

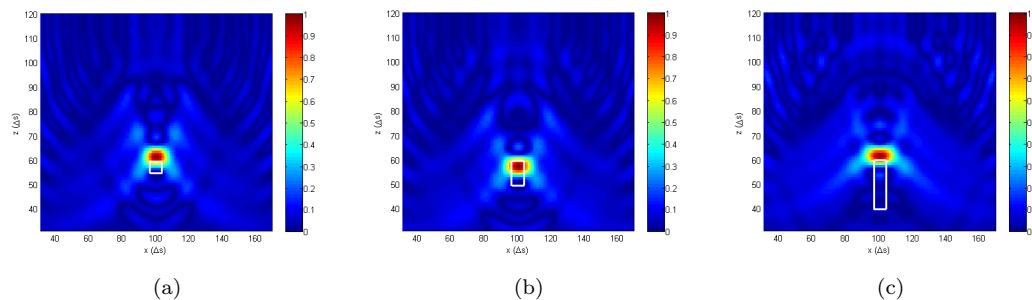


Figure A6. Images of the first singular vectors of co-range extended dielectric targets. (a) $l_z = 5\Delta_s$. (b) $l_z = 10\Delta_s$. (c) $l_z = 20\Delta_s$. The actual targets are indicated by white rectangles.

Table A2. Actual vs. estimated electrical lengths of extended dielectric targets with different co-range lengths

l_z/Δ_s	5	10	20
actual l_z/λ	0.29	0.58	1.15
estimated l_z/λ	0.289	0.5	0.96
% error	0.3	13	16

Fig. A5(a) and (b) show the spectra of the first and second singular values, respectively, of three dielectric targets with different co-range dimensions. The targets have the same relative permittivity $\epsilon_r = 3$ and the same cross-range length $l_x = 5\Delta_s$. The co-range lengths are 5, 10 and $20\Delta_s$. Again, the valleys frequencies can be used to estimate the co-range electrical length. Actual and estimated values are summarized in Table A2.

It is interesting to note that the spectra of the second singular values are “complementary” to the first singular values, in the sense that they have the spectra of the transmission coefficients through the dielectric targets. The images of the first singular vectors are shown in Fig. A6. Note that they are all located at the top faces of the targets (those facing the array).

(c) *Cross-range extension effect:*

Fig. A7 shows the spectra of the first four singular values of three dielectric targets with different cross-range dimensions. The targets have same relative permittivity $\epsilon_r = 3$ and the same co-range length $l_z = 10\Delta_s$. The cross-range lengths are 20, 40 and $80\Delta_s$, respectively. It can be observed that the number of significant singular values depends on the cross-range extension. The first target has two significant singular values, the second has three, and the third has four. All

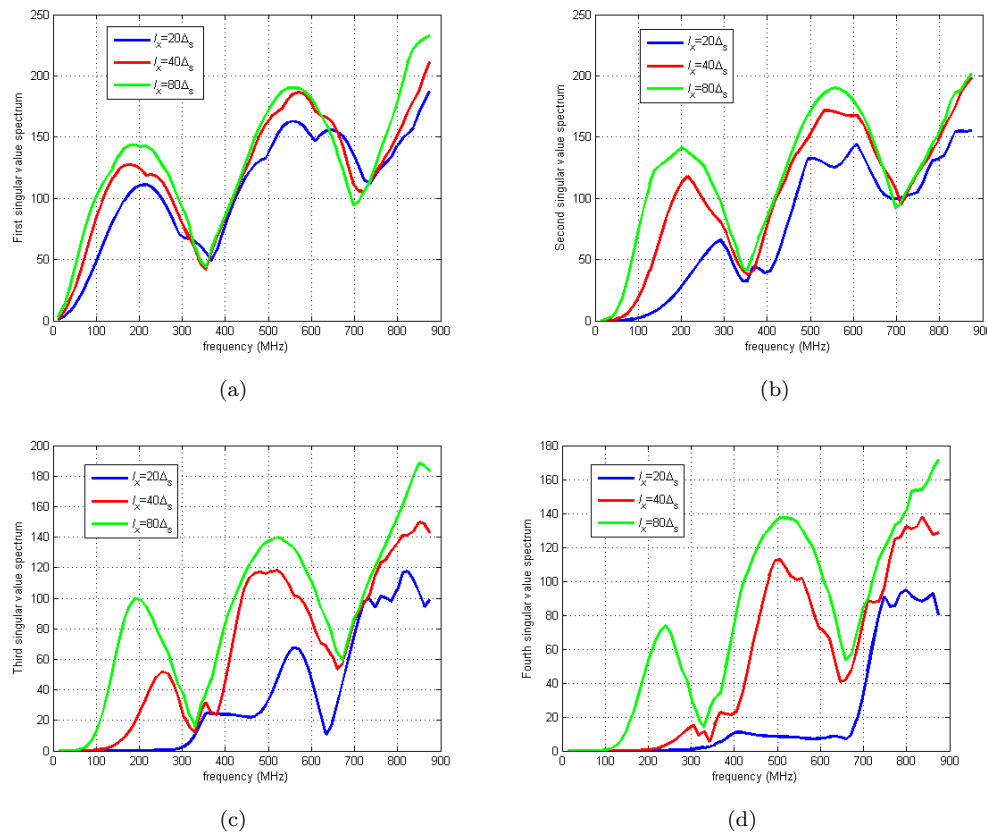


Figure A7. Singular values spectra of cross-range extended dielectric targets with similar permittivities and $l_z = 10$. (a) First (b) Second (c) Third (d) Fourth singular values.

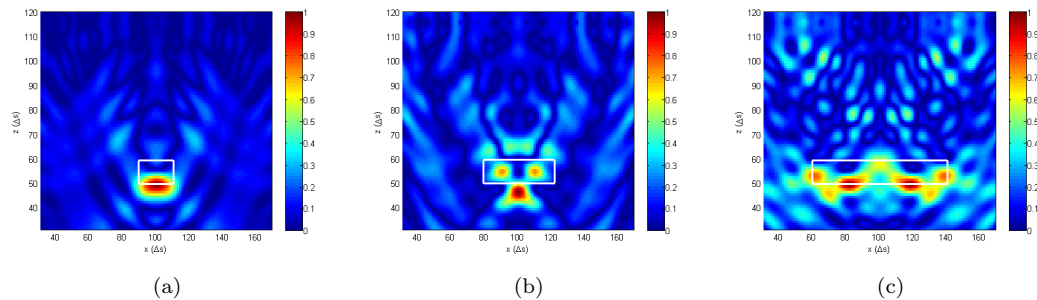


Figure A8. Images of the sum of the significant singular vectors of cross-range extended dielectric targets. (a) $l_x = 20\Delta_s$. (b) $l_x = 40\Delta_s$. (c) $l_x = 80\Delta_s$. The actual targets are indicated by white rectangles.

significant singular values have similar spectrum, from which the co-range length can be estimated.

The images of the sum of the significant singular vectors of each target are shown in Fig. A8. They span the shapes of the respective targets reasonably well.